Optically Detected Magnetic Resonance on Carbene Molecular Qubits

Simon Roggors,[†,‡,¶] Nico Striegler,[†,‡,¶] Thomas Unden,[†] Oleksiy Khavryuchenko,[†,§,‖] Alon Salhov,[⊥,†] Jochen Scharpf,[†] Martin B. Plenio,[#,¶] Alex Retzker,[⊥] Fedor Jelezko,[‡,¶] Matthias Pfender,[†] Philipp Neumann,[†] Tim R. Eichhorn,[†] Tobias A. Schaub,[*,†,‡,¶] and Ilai Schwartz[*,†]

†*NVision Imaging Technologies GmbH, Ulm, Germany*
‡*Institute for Quantum Optics (IQO), Ulm University, 89069 Ulm, Germany*
¶*Center for Integrated Quantum Science and Technology (IQST), 89069 Ulm, Germany*
§*Shupyk National Healthcare University of Ukraine, Kyiv, Ukraine*
‖*Institute of Organic Chemistry of the National Academy of Sciences of Ukraine, Kyiv, Ukraine*
⊥*Racah Institute of Physics, The Hebrew University of Jerusalem, Jerusalem 9190401, Israel*
#*Institute of Theoretical Physics, Ulm University, 89069 Ulm, Germany*

E-mail: tobias.schaub@nvision-imaging.com; ilai@nvision-imaging.com

Abstract

Solid-state quantum systems that utilize optical and spin degrees of freedom in a spin–photon interface have found widespread application in emerging quantum technologies. Recently, molecular qubits have gained center stage as precisely tunable entities that present a compelling alternative to well-established, yet structurally less flexible point defects in solid-state systems. In this work, we disclose ground-state triplet (GST) carbenes embedded in a molecular matrix as organic qubits comprising two unpaired electrons in close proximity that can be optically initialed and read out. *In-situ* photoactivation enables the precise allocation of the carbene position and tuning of its density in the crystalline matrix and lays the ground for optically detected magnetic resonance (ODMR) with high fluorescence contrast of more than 40%, as well as record-high spin coherence times for a molecular spin–photon interface of $T_2 = 157(4)\,\mu\mathrm{s}$ at a temperature of around 5 K. In addition, we show how state-of-the-art quantum chemical calculations including multiscale geometry predictions and complete active space self-consistent field (CASSCF) computations offer comprehensive insight into fundamental spin characteristics. With that, for the first time a series of attractive properties could be united in a single solid-state qubit material: Exclusive usage of light elements (C,H,O,N), optical spin-selective excitations and relaxation pathways, and large zero-field splitting (ZFS) parameters on the order of a few GHz resulting in protection against decoherence sources at low magnetic fields. In this study, we take first steps into a hitherto dormant playground for the design and fabrication of molecular solid-state color centers made of purely organic compounds.

Introduction

Owing to their unique characteristics, unpaired electron spins have found widespread application in quantum technologies including quantum computing,[1,2] quantum sensing,[3–5] and quantum communication.[6,7] A leading strategy to such electron spins accessible to experimentalists relies on the coupling of the electron spin to the optical manifold of a color center in a crystalline material. Such spin–photon interfaces have been demonstrated to enable optical initialization, microwave control, and optical read-out of individual quantum systems using ODMR.[8–10] By far the best studied system is the nitrogen-vacancy defect (NV) in diamond,[11] followed by other point-defects in semiconductor materials (*e.g.*, silicon,[12] and silicon carbide[13]). However, owing to their intrinsic structural fixedness, property tuning poses a long-standing challenge for these solid-state materials.

Molecular electron spin systems, on the other hand, have only recently emerged as potential quantum materials that unite the best of two worlds: The favorable optical and spin properties of defect-based solid-state system and the structural flexibility associated with molecular entities that can be prepared by atom-precise bottom-up synthesis and then self-assembled to provide well-defined crystalline systems.[14–16] In line with these efforts, a series of seminal reports have recently exploited organometallic Cr^{4+}-based complexes with a GST to demonstrate ODMR[17] and showed up ways to further enhance coherence times by subtle modification of the molecular qubit[18] and the surrounding molecular matrix.[19 20] Despite the presence of a heavy atom center and the associated strong spin–orbit coupling (SOC), these organometallic systems reached remarkable T_2 coherence times up to 10.6 µs at a temperature of 4 K[20] by taking advantage of triplet clock transitions at zero magnetic field suppressing decoherence due to the nuclear spin environment. ODMR was also demonstrated for purely organic diradical molecules based on triphenylmethyl radical center.[21] However, their inherently small ZFS parameters prevent spin-selective optical excitation and due to the low spin-selectivity of the intersystem crossing (ISC) between the triplet and singlet manifolds, only low ODMR contrasts of 5×10^{-4} could be achieved. In addition, a fairly small exchange coupling in the single-digit meV regime leads to nearly degenerate singlet–triplet energies, resulting in a low spin-polarization in the triplet ground state.

To date a molecular platform that is able to unify the aforementioned characteristics – large ZFS parameter in the GHz regime, spin selective excitations and relaxation pathways, large singlet triplet gaps, and long coherence times – is still elusive. With this in mind, we set out to explore carbenes in the context of quantum technology applications as a class of diradicals in which the two unpaired electrons are formally confined at the closest possible distance, *i.e.* on a single carbon atom.

In the following, we discuss the design principles, quantum computational property prediction, realization, and in-depth characterization of a purely organic molecular spin system based on a diarylcarbene, namely 2,2'-dinaphthylcarbene (DNC), which has been embedded in a structurally related crystalline 2,2'-dinaphthylketone (DNK) matrix. This molecular quantum material imparts large ZFSs (longitudinal and transversal) in the GHz regime, which enables protection against decoherence sources at low magnetic fields and allowed us to experimentally realize optical spin-selective excitations with high ODMR contrasts. We combine these excellent optical and coherence properties with spatially controllable photoactivation to control the local distribution and density of the triplet-state molecules and further reduce the impact of the surrounding nuclear spin bath on the observed coherence time using perdeuterated DNC-d_{14} in DNK-d_{14} crystals.

Results and discussion

Material design and modeling

Owing to their unpaired electrons, unprotected GST diarylcarbenes are well-known for their high reactivity with lifetimes not exceeding µs in most cases, which precludes their direct application to fabricate solid-state quantum materials from solution.[22,23] Fundamental photophysical and magnetic properties of DNC have been first reported us-

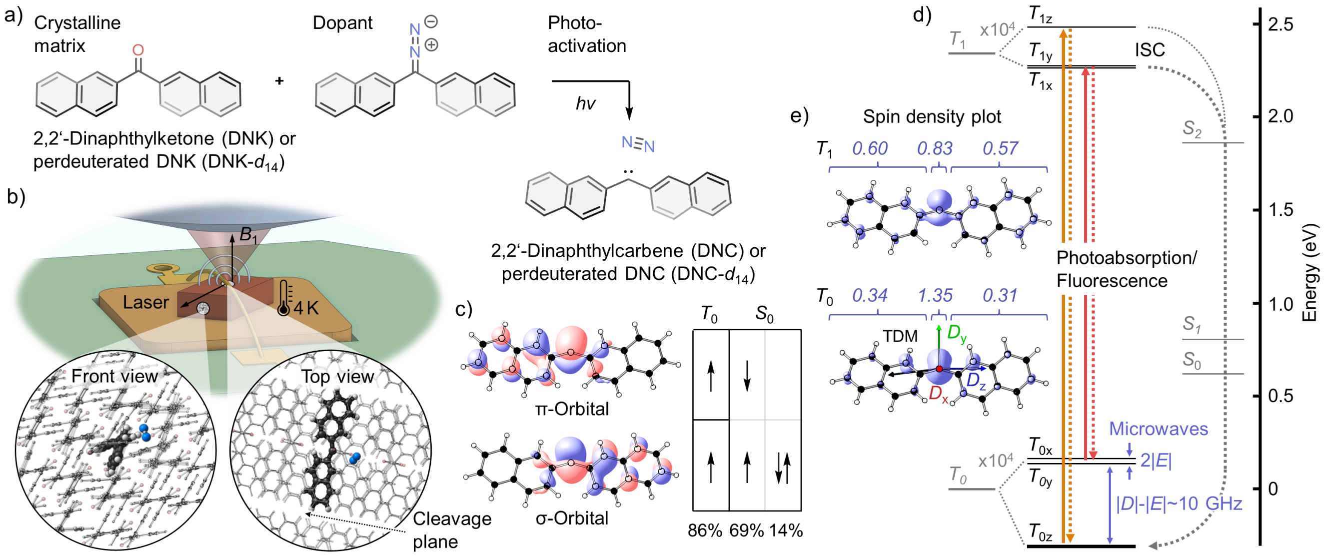

Figure 1: DNC-in-DNK molecular crystals as a quantum–technology platform using a spin–photon interface. a) Molecular components and photoactivation. b) Sketch of the cryogenic confocal microscope with microwave access focused on a DNC-in-DNK crystal; top and front view to illustrate the crystal structure and orientation on the sample stage together with optical and microwave (B_1) polarization. c) Spin-bearing σ and π orbitals (isosurface=0.03) of the GST and GSS. d) Energy level scheme (to scale, ZFS enlarged) with spin–photon interface provided by a substantial change of the ZFS between ground and photoexcited triplet states, and the mechanism of optical initialization by selective ISC from photoexcited spin states $T_{1\mathrm{x}}$ and $T_{1\mathrm{y}}$ to the ground spin state $T_{0\mathrm{z}}$ via the singlet spin manifold. e) Spin-density plots (isosurface=0.008) of T_0 and T_1 together with the orientation of the ZFS tensor and the transition dipole moment (TDM) from CASSCF/NEVPT2 calculations (see SI, Sec. 4.2.5–4.2.7). Numbers denote the overall spin densities of the naphthyls and the carbene center.

ing a photoactivation strategy of the corresponding diazo precursor at cryogenic temperatures in frozen solution (Shpol'Skii matrices).[24–26] By contrast, we employ a structurally related DNK matrix and embed the isolable 2,2'-dinaphthyldiazomethane precursor using solution-phase crystal growth methods to furnish dilute molecular crystals.[27–31] In its crystalline state DNK adopts a laminar arrangement in which the individual layers are held together by weak dispersion interactions. The formation of layers is dictated by comparatively strong antiparallel dipolar ketone as well as C=O$\cdots$H–C interactions and numerous C–H$\cdots\pi$ interactions resulting in a tightly packed edge-to-face arrangement of the naphthyls devoid of π-π stacking (see Sec. 3 in the SI). By virtue of comparable molecular dipole moments and structural resemblance of the ketone matrix and diazomethane dopant, this substitutional doping strategy allows us to precisely define the orientation and environment of the qubits within the crystal lattice. Under cryogenic conditions, the embedded carbene precursor can then be photoactivated[32,33] to generate a nitrogen molecule and a GST DNC, both of which remain trapped in the tightly packed crystal lattice (fig. 1a), see also Sec. 5.1.1 in the SI).[34]

In order to account for the confining impact of the crystalline DNK lattice on the molecular shape of DNC, a co-crystal model was derived and optimized in a two-step protocol using quantum computational methods. First, the geometry-relaxed matrix system was obtained from multiscale ONIOM optimization[35] implemented in Gaussian 16,[36] with density functional theory (DFT) treatment for a central DNC and nitrogen and semi-empirical treatment for two shells of surrounding DNK matrix molecules (1909 atoms in total, for computational details see Sec. 5 of the SI). In the second step, an extracted model including DNC, nitrogen, and six surrounding matrix molecules was subjected to constrained optimization at the PBE0/def2-TZVP-D3 level of theory[37] . Finally, multireference calculations as implemented in ORCA version 5.0.3[38,39] were conducted on the resulting DNC geometry for property prediction. Here we rely on state-averaged CASSCF[40] calculations (averaging three lowest triplet and five singlet states) with ten electrons in ten orbitals. Perturbative treatment within the N-electron valence-state second-order perturbation theory (NEVPT2)[41 42 43] in conjunction with quasidegenerate perturbation theory (QDPT)[44] were performed to further refine all energies and account for scalar relativistic and SOC effects. In agreement with recent reports,[45] we find DNC to adopt a bent conformation ($\sphericalangle$CCC = 148.0°, fig. 1b) with two orthogonal spin-bearing molecular orbitals (σ and π), as a result of the formal mixing of a 2p orbital at the carbene carbon with an sp orbital to generate an $(\mathrm{sp})^n\mathrm{p}^n$ hybrid valence orbital (fig. 1c).

We find, that DNC comprises a GST that is stabilized by $\sim$ 0.6 eV over the ground state singlet (GSS) form. In a simplified picture, the difference of the electronic wavefunction between the GST and the GSS is predominantly due to the population change of one electron from a π to a spatially orthogonal σ orbital (fig. 1c). When photoexcited, this population change gives a bias towards population of the $T_{0\mathrm{z}}$ spin state of the GST by intersystem crossing (ISC) via perturbative SOC, resulting in optical spin pumping.[45,46] In general, one finds that the photoexcited triplet state decays via the singlet spin manifold predominantly from $T_{1\mathrm{x}}$ and $T_{1\mathrm{y}}$ to $T_{0\mathrm{z}}$, which enables ODMR with high contrast (see fig. 1d, for details see the SI, Sec. 5.2.8). The spin-density plot shows considerable confinement of the unpaired spin on the central carbene carbon in the ground state, which is reflected in strong SOC (predicted ZFS parameter are $\mathrm{D}_0^{\mathrm{theo}} = +11180\,\mathrm{MHz}$ and $\mathrm{E}_0^{\mathrm{theo}} = -340\,\mathrm{MHz}$, fig. 1e) whereas for the first excited triplet state a depletion of spin density in the p-orbital at the central carbon by approx. 42 % leads to a redistribution of spin density, which reduces and even changes the sign of the ZFS parameters to $\mathrm{D}_1^{\mathrm{theo}} = -5120\,\mathrm{MHz}$ and $\mathrm{E}_1^{\mathrm{theo}} = +80$ MHz,[47] and thus provides access to triplet spin states through well-separated optical transitions. Our calculations predict that the axes of the ZFS tensor in the ground and first excited triplet state are co-aligned with a vector projection of > 0.999 (> 0.97) for $T_{0\mathrm{z}}$ ($T_{0\mathrm{x}}$ and $T_{0\mathrm{y}}$), suggesting primarily spin-conserving optical transitions (see the SI, Sec. 5.2.7). Due to the large, anisotropic ZFS coupling ($|D|$, $|E|$ on the order of GHz), we expect suppression of first-order coupling of the electron spin to the magnetic environment by placing the GST in a protected 'clock state' at low magnetic fields which has been reported to increase the spin coherence time T_2.[20,48]

EPR spectroscopy

We start the discussion of our experimental results with a brief description of the sample preparation. All compounds were prepared on a gramm scale in concise batch-type syntheses starting from 2-bromonaphthalene and have been thoroughly purified by sublimation and recrystallization techniques in the final step. Red colored, millimeter-sized dilute molecular crystals of DNC precursor in DNK were grown by slow vapor diffusion of isopropanol into a saturated solution of DNK (0.035 M) and the 2,2'dinaphthyldiazomethane, (0.1-1 mol%) in ethylacetate within several days. Quantitative doping was proven by ^{1}H NMR spectroscopy of as prepared dilute molecular crystals in the doping range from ca. 0.1–10 ppt (see the SI, Sec. 2.2).

Electron paramagnetic resonance (EPR) spectroscopy at cryogenic temperatures was employed to shine light on the photoactivation process and analyze the GST properties of cut and oriented DNC-in-DNK crystals of $\sim$ 1 mm^3 sizes (see fig. 2a and the SI, Sec. 2.1, for details). By probing the emergence of a triplet spin signal, we observe that not only UV-light but also light in the visible spectrum, such as green laser light at 532 nm, can

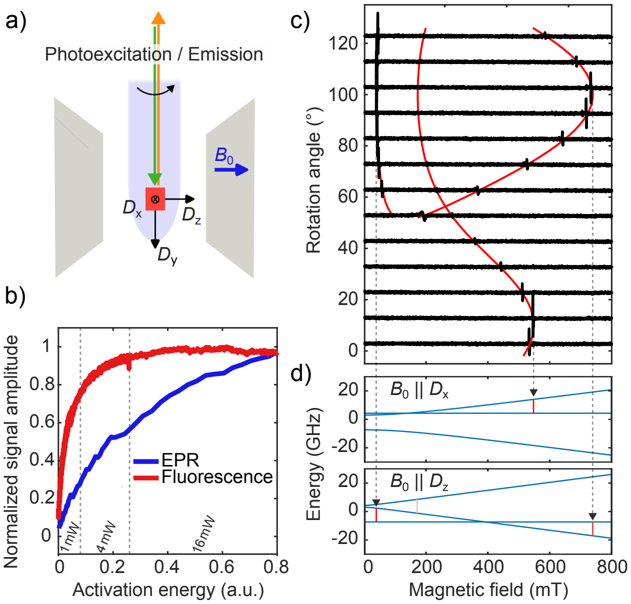

Figure 2: a) Sketch of the EPR setup (see also the SI, Sec. 6.1) combined with optical excitation and fluorescence detection using an optical fiber. b) Simultaneous EPR and fluorescence detection during activation with a 532 nm laser at 20 K, using three different power levels from 1 to 16 mW. Both signal amplitudes are initially correlated. c) X-band (9.72 GHz) magnetic-field-swept CW EPR rotation-dispersion spectrum of an annealed sample (rotation about D_y axis), showing the ZFS anisotropy of the triplet spin resonances in a magnetic field B_0. Simulation of the resonance fields are plotted in red for $(D,\ E)$ = (11000, -650) MHz (absolute values are taken from powder spectra, sign from quantum chemistry calculations (see the SI, Sec. 5.2.7). d) Simulation of triplet levels in an external magnetic field B_0 parallel to D_x and D_z. Vertical lines indicate matches of the resonance field positions with local resonance maxima and minima in the experimental data. All simulations were performed using EasySpin.[49]

be used for photoactivation of DNC (see fig. 2b), providing a direct correlation of EPR signal intensity and fluorescence intensity. However, at larger activation energies, the fluorescence signal saturates while the EPR signal continues to increase, which we assume to be primarily a combined effect due to a discrepancy between optical activation and detection volume, and EPR detection volume. Powder spectra reveal distinct differences of the ZFS tensors between nascent and annealed DNC $((|D|,|E|)_{\mathrm{nasc.}} = (10580, 380)\,\mathrm{MHz} \rightarrow (|D|,|E|)_{\mathrm{ann.}} = (11000, 650)\,\mathrm{MHz})$. As a result, we can follow the conversion from one species to the other in crystalline samples and find the temperature for the onset of annealing at ~140 K and quenching of the spin signal at ~250 K (see SI, Sec. 6.2). ZFS parameters derived from powder spectra were used to simulate rotation-dispersion spectra for crystalline samples[49] which in turn can be compared to experimental data. Hereby, we identify that the slow axis of birefringence n_s within the cleavage plane of DNK appears to coincide with the ZFS tensor axis D_y of DNC (while D_z being normal to the cleavage plane), however, due to the precision of cutting and mounting the sample, within a ~10° certainty (see fig. 2c and d).

Further experimental data on coherence and spin–lattice relaxation times were collected, using a perdeuterated, fully activated and annealed crystal (average distance of 4 nm between DNC-d_{14} molecules, for relation to the dopant density see the SI, Sec. 2.1). Here, the sample was turned along the normal to the cleavage plane to closely match the condition $B_0 \parallel D_\mathrm{y}$, which gives an X-band resonance at ~460 mT. We note that for DNC-d_{14} in DNK-d_{14} the ZFS parameters slightly change to $(|D|,|E|)_{\mathrm{deut.,\ ann.}} = (10991, 651)\,\mathrm{MHz}$. In a two-pulse Hahn-echo measurement at 20 K we found a T_2 of 34 µs on the longer-lifetime component of a biexponential fit, and in an inversion-recovery experiment we obtained curves that can best be fit with an stretched exponential, which shows an increase of T_1 from ~1 ms at 20 K up to ~100 ms at 3.5 K (see the SI, Sec. 6.3, for data and fits).

Optical spectroscopy

The electronic emission spectrum of photoactivated DNC was recorded in frozen 2-methyltetrahydrofuran solution at 77 K (see the SI, Sec. 4). DNC exhibits a main emission band centered at λ_{em} = 604 nm which is followed by two vibronic side bands with decreasing intensity at 650 nm and 720 nm. We observe an increase in the overall photoluminescence quantum yield (PLQY) upon deuteration from $\phi_{\mathrm{PLQY}} = 0.02$ for DNC to 0.03 for DNC-d_{14} due to decrease of internal conversion probability.[50] Given the results from single crystal EPR measurements, doped crystals were cut so that the polarization of excitation laser light can be aligned with the transition dipole moment (TDM) of DNC while the microwave field B_1 couples roughly equally to the two X-band transitions (see fig. 1b and the SI, Sec. 2.1 for details on sample preparation). The crystal was placed inside a laser-scanning confocal microscope with a cold-finger sample mount at a temperature of $\sim 4\,\mathrm{K}$. Optical excitation was performed using a continuous-wave dye laser operating at wavelengths between 570 nm and 620 nm. Fluorescence can either be detected by photon counting or by fluorescence spectrometry. In addition, a copper wire was placed on top of the crystal, conveying alternating magnetic fields to manipulate the electron spin state (see fig. 1 b). The microscope is described in detail in the SI, Sec. 7.

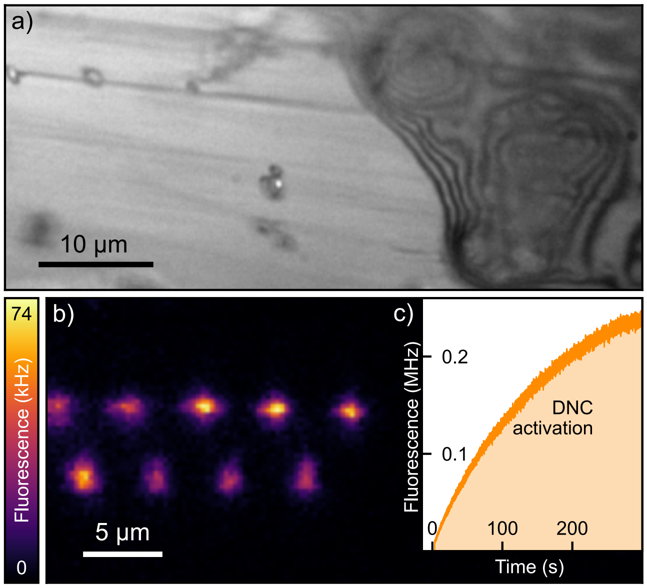

Figure 3: a) Image of a doped crystal surface inside the cryogenic microscope. Illumination performed with red light filtered by a 650 nm longpass. Surface features are a result of the sample manufacture procedure, likely leaving crystalline fragments of various sizes on the surface (see fig. 1b). b) Confocal laser-scanning fluorescence microscopy image of a DNC-in-DNK crystal surface. Illumination with 70 nW of 597.9 nm laser light and detection of 615 nm longpass-filtered fluorescence. The image shows nine regularly arranged, bright spots where DNC molecules in the DNK crystal have been photoactivated. c) Monitoring photoactivation of DNC molecules from their diazo precursors inside the confocal volume of the DNK crystal. The fluorescence count rate is increasing when 5 µW of 570 nm laser light is focused on the surface of the doped DNK crystal.

Figure 3 shows an exemplary white-field image of the crystal surface (upper image). Since the crystal was manually cut surface damage and also chipped crystalline fragments can be observed, particularly on the right-hand side. When tuning the laser wavelength to 570 nm at a laser power of a few µW, illumination of a diffraction limited spot shows an increase in fluorescence over a timescale of seconds to minutes, while prolonged activation quenches the observed fluorescence due to photobleaching effects (inset graph in fig. 3 and the Si, Sec. 7.2). After this photoactivation procedure, local bright spots can be observed with low background fluorescence when tuning the dye laser on resonance with the zero-phonon line (ZPL) of the DNC molecules at 598.0 nm and reducing the excitation power to 70 nW (fig. 3, lower image).

After the activation process, an annealing step is performed by heating the crystal to 200 K for around 30 minutes, in order to allow for structural relaxation of the nascent GST carbene, the nitrogen, and the surrounding matrix (see the SI, Sec. 6.2 for details).[26] Excitation of one of the fluorescent spots with the dye laser set to a wavelength of 580 nm, shows a fluorescence spectrum with ZPLs at 602.8 nm and 600.9 nm for DNC and DNC-d_{14}, respectively (*i.e.*, they are shifted after annealing, see fig. 4a). By exciting only a small subset of the DNC molecules when using low laser power in resonance to the ZPL, the impact of inhomogeneous broadening on the fluorescence spectrum can be reduced,[51] increasing the visibility of the vibrational sidebands.

The optical spectrum is further evaluated by

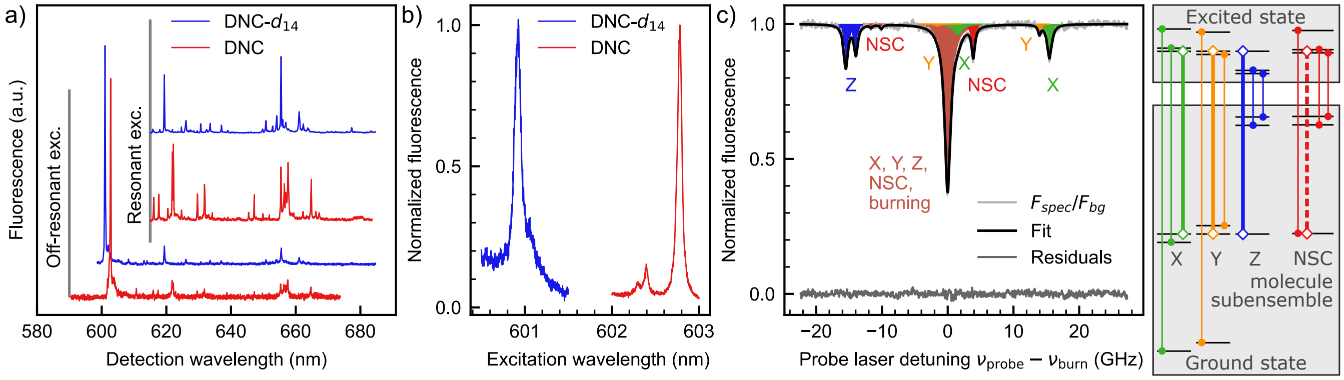

Figure 4: a) Fluorescence spectra of DNC and DNC-d_{14} under off-resonant excitation at 580 nm and under resonant excitation at the ZPL of DNC and DNC-d_{14}. b) Fluorescence excitation spectra around the ZPL of DNC and DNC-d_{14}. The fluorescence is filtered with a 615 nm longpass. c) Spectrum of holes in the ZPL of DNC in DNK after "burning" for ∼ 60 s with 500 nW of laser light at ν_{burn}. The plot shows the fluorescence for a scan of the 50 nW probe laser frequency ν_{probe} across part of the ZPL (for normalization see the SI, Sec. 7.4). Ten Lorentzian dips have been fit to the data (residuals shown). Each Lorentzian is assigned to an optical transition depicted as vertical lines in the energy level diagrams on the right. The energy levels of the four subensembles of DNC molecules are marked X, Y, Z and NSC. Each subensemble has an optical transition in resonance with the burning laser (bold, vertical line with open diamond marker). These are spin-conserving for $T_{0\text{x}} \leftrightarrow T_{1\text{x}}$, $T_{0\text{y}} \leftrightarrow T_{1\text{y}}$ and $T_{0\text{z}} \leftrightarrow T_{1\text{z}}$ and non-spin-conserving for $T_{0\text{z}} \leftrightarrow T_{1\text{x}}$ (NSC molecules, dashed line, see the SI, Sec. 7.4).

performing laser excitation spectroscopy, where the longpass-filtered fluorescence intensity is measured while varying the output wavelength of the excitation laser by 1 nm around the ZPL of the DNC molecules. The resulting spectra show an inhomogeneously broadened resonance at 600.9(1) nm for DNC-d_{14} and 602.8(1) nm for DNC, with a full-width at half maximum (FWHM) of ∼ 80 GHz and ∼ 50 GHz, respectively. For the spectrum of DNC, the small peak at slightly higher excitation energies is ascribed to phonon sidebands.

When exciting the annealed DNC molecules at a wavelength of 602.8 nm and an increased illumination power of 500 nW for around 60 seconds, the formation of a spectrally burned hole and associated satellite is observed.[24–26] This spectrum can be explained by considering four different molecule classes with different burning transitions in resonance with the burning laser, as shown in fig. 4c. Three of the molecule groups, labeled X, Y and Z correspond to a subensemble of the inhomogeneously broadened ensemble, where the $T_{0\text{x}} \rightarrow T_{1\text{x}}$, the $T_{0\text{y}} \rightarrow T_{1\text{y}}$ and the $T_{0\text{z}} \rightarrow T_{1\text{z}}$ optical transition are in resonance with the burning laser, respectively. In addition, another optical excitation from $T_{0\text{z}}$ to $T_{1\text{x}}$ or $T_{1\text{y}}$ has to be considered to explain the full hole spectrum. From the spectral positions of the holes and the predetermined values for the ZFS in the ground state, the excited state ZFS D_{ES} = -3.735 GHz and E_{ES} = 0.082 GHz can be deduced (for full analysis see the SI, Sec. 7.4).

Optically detected magnetic resonance

In order to investigate the properties of the GST, as well as the possibility for ODMR, we apply microwave signals to the microwave stripline placed across the crystal. When exciting the DNC molecules with continuous laser excitation resonant to the ZPL at 602.8 nm while at the same time sweeping the applied microwave frequency, a sharp increase of fluorescence can be observed at microwave frequencies of 10.3101 GHz and 11.6053 GHz, which corresponds to the $T_{0\text{z}} \rightarrow T_{0\text{y}}$ and $T_{0\text{z}} \rightarrow T_{0\text{x}}$ spin transition, respectively ($\rightarrow D_{\text{GS}}^{\text{exp}} = 10.958\,\text{GHz}$,

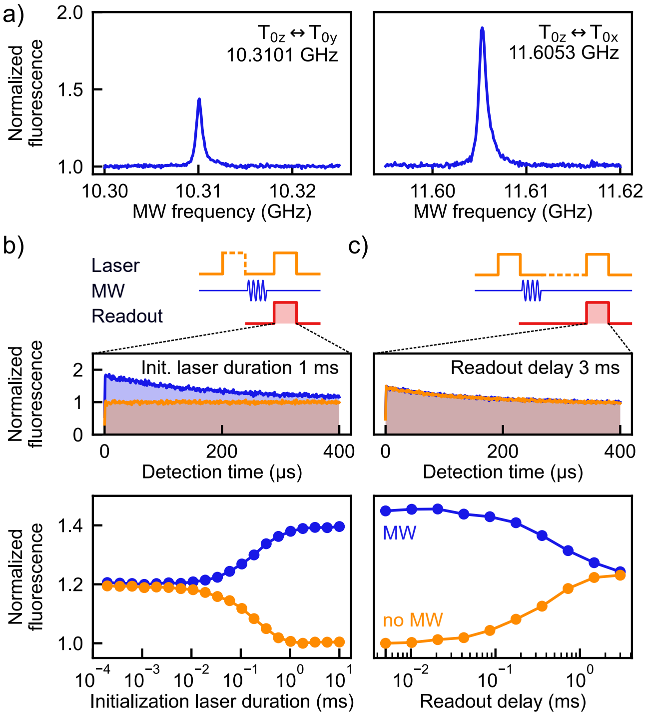

Figure 5: ODMR on DNC in DNK. (a) Continuous resonant laser excitation (602.8 nm, 50 nW) and a microwave field with variable frequency reveal fluorescence peaks when the microwave frequency is in resonance with the spin transitions $T_{0z} \leftrightarrow T_{0y}$ or $T_{0z} \leftrightarrow T_{0x}$. (b) Pulsed spin initialization and readout protocol: After a 5 ms dark thermalization period a spin initialization laser pulse with variable duration is applied,[17,52] followed by a resonant microwave $\pi-$pulse on the $T_{0z} \leftrightarrow T_{0x}$ transition (or none for reference). Finally, a 400 µs readout laser pulse induces a fluorescence response. Two exemplary responses are displayed vs. detection time, one for the case with (blue) and one without (orange) microwave pulse. The averaged responses is plotted vs. different initialization laser pulse durations. (c) Delaying the readout laser pulse reveals the accessible lifetime of the optically prepared spin state. For a delay of 3 ms the fluorescence response with (blue) and without (orange) microwave pulse coincide. In order to highlight the magnitude of the ODMR effect, fluorescence is normalized to the continuous-excitation fluorescence level.

$E_{\mathrm{GS}}^{\mathrm{exp}} = -0.648\,\mathrm{GHz}$).

More elaborate pulsed-ODMR schemes are possible once the time-dependent optical spin polarization and depolarization are evaluated. In figure 5b we show experiments in which an initialization laser pulse was varied in duration, followed by either a microwave pulse of duration 88 ns (corresponding to a rotation of π according to the Rabi-oscillations measurement, fig. 6a), or a waiting time of same length. The fluorescence response following a readout laser pulse (400 µs duration) is accumulated over several runs and shows an effective laser-induced spin polarization that saturates after about 1 ms (see Sec. 7.5 in the SI).

When keeping the initialization laser pulse at a constant length of 1 ms and varying the time between initialization and readout laser pulse, the observable ODMR signal vanishes with a decay time of 0.58(1) ms. The discrepancy between this value and $T_{1,\mathrm{EPR}} \sim 100\,\mathrm{ms}$ is mostly governed by an inaccuracy of the measured temperature, and discussed in the SI, Sec. 7.6.

Having established a generalized measurement sequence consisting of a 1 ms spin initialization laser pulse, followed by a spin-manipulation time of up to 0.58(1) ms and a readout laser pulse with a length of 400 µs, the properties of the electron spin can be probed further. By setting the microwave frequency to 11.6053 GHz and varying the duration of the microwave pulse,[53] coherent Rabi oscillations of the spin state between T_{0z} and T_{0x} can be observed, with a Rabi frequency of 5.2 MHz, from which the pulse length for π and $\pi/2$ rotations are derived (fig. 6a).

For electron spins in solid-state systems, spin coherence times are typically adversely affected by the nuclear[54] and electron spin environment.[55,56] For DNC in DNK, this mainly involves the proton nuclear spin environment, as well as the electron spins of other nearby DNC molecules. In the special case of zero magnetic field in combination with large D_{gs} and E_{gs} values, the effect of the nuclear spin bath on the electron spin coherence can be significantly different from the case of non-zero magnetic fields.[20] To quantify the effects, a DNC-in-DNK crystal is compared to DNC-d_{14} in DNK-d_{14} (fig. 6b). An increase of the coherence time by one order of magnitude is observed for full deuteration, owing to the gyromagnetic ratio

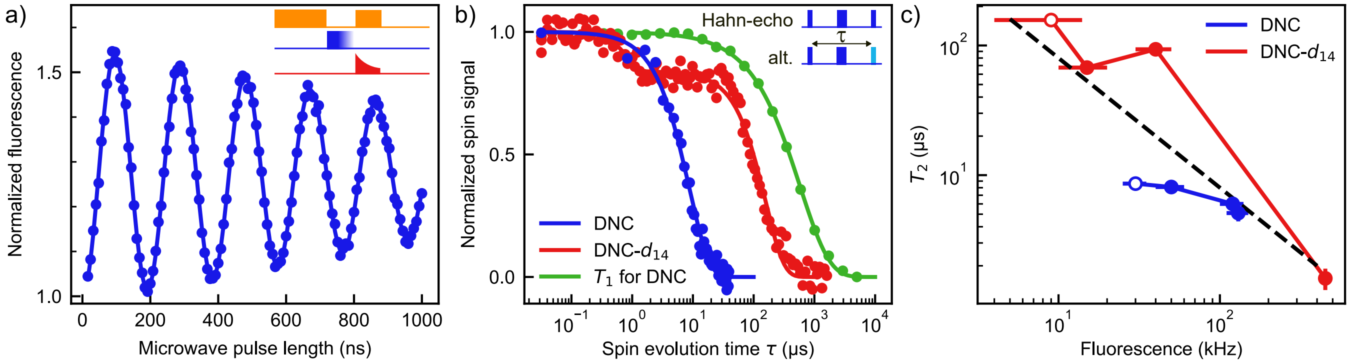

Figure 6: Coherent spin manipulation of DNC in DNK. a) Rabi oscillations on spin transition T_{0z} to T_{0x}. The pulse sequence starts with an initial laser pulse, followed by a microwave pulse of variable duration, a 400 µs readout laser pulse and a waiting time of 5 ms (see inset). The sum of all fluorescence photons during a readout laser pulse is normalized to the signal without microwave and is plotted over the duration of the microwave pulse. A damped-cosine fit to the data yields a Rabi frequency of 5.207(4) MHz. b) Hahn-echo measurements on DNC and DNC-d_{14}. The microwave sequence consists of a $\pi-$pulse centered between two $\pi/2$ pulses resonant to the Z–X transition. Consecutive pulse sequences alternate the phase of the final $\pi/2$ pulse between 0 and π (color change in pulse sequence in inset). The corresponding fluorescence data is subtracted, and the result normalized. The sequences loop over the delay τ between the two $\pi/2$ pulses. An exponential decay function is fitted to the normalized data and yields coherence times $T_2 = 8.6(3)$ µs and 157(4) µs for DNC and DNC-d_{14}, respectively. For the DNC-d_{14}, a double exponential is fitted to the data and the longest time presented. For comparison, the plot shows the decay of available spin polarization as in figure 5c. c) The Hahn-echo T_2 times for DNC and DNC-d_{14} for different levels of local DNC activation. The degree of activation is expressed by the level of fluorescence count rate I_{PL} under 5 µW, 570 nm laser excitation at the respective locations. The open circles correspond to the data extracted from Hahn-echo measurements in panel b. The dashed line is a guide to the eye for $T_2 \propto I_{\mathrm{PL}}^{-1}$.

of a deuterium nuclear spin being more than six times smaller than that of a proton nuclear spin. For the DNC-d_{14}-in-DNK-d_{14} crystal we measure the highest T_2 time to be 157(4) µs at a temperature of 5 K (or higher, see Sec. 7.6 in the SI).

As 2,2'-dinaphthyldiazomethane does not possess an unsaturated electron spin, the effective electron-spin density can be controlled *in-situ* by partial photoactivation, with an upper accessible limit equal to the formal dopant density of the diazo precursor. When quantifying the partial activation process by measuring the fluorescence count rate I_{PL} after the activation process, higher T_2 times are observed for lower photoactivation levels, due to a lower electron spin density (see fig. 6c). As mutual interactions between DNC electron spins influence T_2 and these interactions scale proportional to the density of DNC, a guide to the eye for $T_2 \propto I_{\mathrm{PL}}^{-1}$ is included in fig. 6c. While our data for DNC-d_{14} roughly follows this trend, we find the effect of varying electron spin density to be less pronounced for DNC. We attribute this suppression to the more pronounced decoherence due to proximal proton spins in the case of DNC. This method can only provide qualitative results, as it does not allow quantification of the actual resulting electron spin densities. Future experiments should include electron–electron double resonance spectroscopy to determine the actual electron–spin density.[57]

Conclusion

We communicate the design and experimental realization of a novel organic molecular material with a spin–photon interface enabling spin-selective electronic excitation and relaxation schemes that permit for the first time ODMR with high contrast by optical spin pumping ($> 40\%$). By virtue of strong ZFS, the absence of heavy atoms, and deuteration of dopant and matrix, our crystalline qubit material features remarkable spin coherence times of $T_2 = 157(4)\,\mu s$ at zero magnetic field and a temperature of $\geqq\ 5\,K$ which constitutes an improvement of more than one order of magnitude compared to previously reported molecular qubits.[20] In addition, the applied photoactivation protocol using a confocal microscope, permits precise control over the spatial distribution and density of the triplet-state electron spins. This strategy unlocks opportunities in the fabrication of integrated device architectures by co-localizing tailored patterns of carbene molecules with optical, magnetic or electric interfaces at the nanometer scale.[58–61] We show how state-of-the-art multireference quantum chemical calculations can be used to predict relevant quantum properties, which is of particular importance to speed up the progress in the development of novel molecular materials using computationally guided molecular design. It is worth mentioning that the strategy of embedding an isolable diaryldiazomethane precursor into a structurally related diarylketone with subsequent photoactivation under cryogenic conditions is universally applicable and is currently being pursued to access a new family of solid-state color centers with enhanced optical and spin properties tailored to the application in quantum technology.

Acknowledgement The authors acknowledge support by the state of Baden-Württemberg through bwHPC and the German Research Foundation (DFG) through grant no INST 40/575-1 FUGG (JUSTUS 2 cluster). The work was furthermore made possible by the DLR Quantum Computing Initiative and the Federal Ministry for Economic Affairs and Climate Action (COMIQC project, https://qci.dlr.de/projects/COMIQC). A.S. gratefully acknowledges the support of the Clore Israel Foundation Scholars Programme, the Israeli Council for Higher Education, and the Milner Foundation. Mass spectrometry and X-ray crystallography was conducted at the Service Center mass spectrometry and X-ray crystallography facility at the University of Ulm. Photoluminescent quantum yields were recorded at the Institute for Organic Chemistry III, University of Ulm. The authors would further like to thank Dr. P. Hautle, Paul Scherrer Institute, Switzerland, for loaning of the EPR cryostat and Dr. Mathias Hermann (Institute of Organic Chemistry II and Advanced Materials, Ulm University) for X-ray crystallographic analysis.

Supporting Information Available

Supporting Information including details of synthetic and experimental procedures, crystal fabrication, X-ray crystallographic data, bulk optical spectroscopy data, quantum chemical calculations, EPR spectroscopy analysis, further optical spectroscopic data and analysis is available. Deposition Number 2443791 (DNK) and 2443792 (DNK-d_{14}) contains the supplementary crystallographic data for this paper. These data can be obtained free of charge via the joint Cambridge Crystallographic Data Centre (CCDC) and Fachinformationszentrum Karlsruhe Access Structures service under https://www.ccdc.cam.ac.uk/structures. Gaussian and ORCA output files are uploaded as separate files and can be found under https://www.dx.doi.org/10.6084/m9.figshare.28854836

References

(1) Dutt, M. V. G.; Childress, L.; Jiang, L.; Togan, E.; Maze, J.; Jelezko, F.; Zibrov, A. S.; Hemmer, P. R.; Lukin, M. D. Quantum Register Based on Individual Electronic and Nuclear Spin Qubits in Diamond. *Science* **2007**, *316*, 1312–1316.

(2) Neumann, P.; Kolesov, R.; Naydenov, B.; Beck, J.; Rempp, F.; Steiner, M.; Jacques, V.; Balasubramanian, G.;

Markham, M. L.; Twitchen, D. J.; Pezzagna, S.; Meijer, J.; Twamley, J.; Jelezko, F.; Wrachtrup, J. Quantum register based on coupled electron spins in a room-temperature solid. *Nature Physics* **2010**, *6*, 249–253.

(3) Maze, J. R.; Stanwix, P. L.; Hodges, J. S.; Hong, S.; Taylor, J. M.; Cappellaro, P.; Jiang, L.; Dutt, M. V. G.; Togan, E.; Zibrov, A. S.; Yacoby, A.; Walsworth, R. L.; Lukin, M. D. Nanoscale magnetic sensing with an individual electronic spin in diamond. *Nature* **2008**, *455*, 644–647.

(4) Dolde, F.; Fedder, H.; Doherty, M. W.; Nöbauer, T.; Rempp, F.; Balasubramanian, G.; Wolf, T.; Reinhard, F.; Hollenberg, L. C. L.; Jelezko, F.; Wrachtrup, J. Electric-field sensing using single diamond spins. *Nature Physics* **2011**, *7*, 459–463.

(5) Wu, Y.; Jelezko, F.; Plenio, M. B.; Weil, T. Diamond Quantum Devices in Biology. *Angewandte Chemie International Edition* **2016**, *55*, 6586–6598.

(6) Bernien, H.; Hensen, B.; Pfaff, W.; Koolstra, G.; Blok, M. S.; Robledo, L.; Taminiau, T. H.; Markham, M.; Twitchen, D. J.; Childress, L.; Hanson, R. Heralded entanglement between solid-state qubits separated by three metres. *Nature* **2013**, *497*, 86–90.

(7) Hensen, B. et al. Loophole-free Bell inequality violation using electron spins separated by 1.3 kilometres. *Nature* **2015**, *526*, 682–686.

(8) Suter, D. Sensitivity of optically excited and detected magnetic resonance. *Journal of Magnetic Resonance (1969)* **1992**, *99*, 495–506.

(9) Wrachtrup, J.; Von Borczyskowski, C.; Bernard, J.; Orrit, M.; Brown, R. Optical detection of magnetic resonance in a single molecule. *Nature* **1993**, *363*, 244–245.

(10) Awschalom, D. D.; Hanson, R.; Wrachtrup, J.; Zhou, B. B. Quantum technologies with optically interfaced solid-state spins. *Nature Photonics* **2018**, *12*, 516–527.

(11) Gruber, A.; Dräbenstedt, A.; Tietz, C.; Fleury, L.; Wrachtrup, J.; Borczyskowski, C. v. Scanning Confocal Optical Microscopy and Magnetic Resonance on Single Defect Centers. *Science* **1997**, *276*, 2012–2014.

(12) Higginbottom, D. B. et al. Optical observation of single spins in silicon. *Nature* **2022**, *607*, 266–270.

(13) Nagy, R.; Widmann, M.; Niethammer, M.; Dasari, D. B. R.; Gerhardt, I.; Soykal, Ö. O.; Radulaski, M.; Ohshima, T.; Vučković, J.; Son, N. T.; Ivanov, I. G.; Economou, S. E.; Bonato, C.; Lee, S.-Y.; Wrachtrup, J. Quantum Properties of Dichroic Silicon Vacancies in Silicon Carbide. *Physical Review Applied* **2018**, *9*, 034022.

(14) Gaita-Ariño, A.; Luis, F.; Hill, S.; Coronado, E. Molecular spins for quantum computation. *Nature Chemistry* **2019**, *11*, 301–309.

(15) Wasielewski, M. R. et al. Exploiting chemistry and molecular systems for quantum information science. *Nature Reviews Chemistry* **2020**, *4*, 490–504.

(16) Serrano, D.; Kuppusamy, S. K.; Heinrich, B.; Fuhr, O.; Hunger, D.; Ruben, M.; Goldner, P. Ultra-narrow optical linewidths in rare-earth molecular crystals. *Nature* **2022**, *603*, 241–246.

(17) Bayliss, S. L.; Laorenza, D. W.; Mintun, P. J.; Kovos, B. D.; Freedman, D. E.; Awschalom, D. D. Optically addressable molecular spins for quantum information processing. *Science* **2020**, *370*, 1309–1312.

(18) Laorenza, D. W.; Kairalapova, A.; Bayliss, S. L.; Goldzak, T.; Greene, S. M.;

Weiss, L. R.; Deb, P.; Mintun, P. J.; Collins, K. A.; Awschalom, D. D.; Berkelbach, T. C.; Freedman, D. E. Tunable Cr^{4+} Molecular Color Centers. *Journal of the American Chemical Society* **2021**, *143*, 21350–21363.

(19) Baldinelli, L.; Sorbelli, D.; Toriyama, M.; Bistoni, G.; De Angelis, F.; Galli, G. Design Rules to Engineer the Spin Structure of Cr4+ Molecular Qubits via Matrix Modularity. 2025; `https://chemrxiv.org/engage/chemrxiv/article-details/67ca1cf06dde43c908d15baf`.

(20) Bayliss, S. L.; Deb, P.; Laorenza, D. W.; Onizhuk, M.; Galli, G.; Freedman, D. E.; Awschalom, D. D. Enhancing Spin Coherence in Optically Addressable Molecular Qubits through Host-Matrix Control. *Physical Review X* **2022**, *12*, 031028.

(21) Kopp, S. M.; Nakamura, S.; Phelan, B. T.; Poh, Y. R.; Tyndall, S. B.; Brown, P. J.; Huang, Y.; Yuen-Zhou, J.; Krzyaniak, M. D.; Wasielewski, M. R. Luminescent Organic Triplet Diradicals as Optically Addressable Molecular Qubits. *Journal of the American Chemical Society* **2024**, *146*, 27935–27945.

(22) Bertrand, G. *Carbene Chemistry: From Fleeting Intermediates to Powerful Reagents*, 1st ed.; Taylor & Francis Group: Baton Rouge, 2002.

(23) Hirai, K.; Itoh, T.; Tomioka, H. Persistent Triplet Carbenes. *Chemical Reviews* **2009**, *109*, 3275–3332.

(24) Kozankiewicz, B.; Aloshyna, M.; Orrit, M.; Tamarat, P.; Gudmundsdottir, A. D.; Platz, M. S. A Hole-Burning Study of the Zero-Field Splitting of the Triplet Ground and Excited States of 2,2-Dinaphthylcarbene in n-Heptane and n-Hexane at 1.7 K. *The Journal of Physical Chemistry A* **2000**, *104*, 7464–7468.

(25) Kozankiewicz, B.; Gudmundsdottir, A.; Orrit, M.; Platz, M.; Tamarat, P. Hole burning on a triplet–triplet transition: 2,2-dinaphthylcarbene in n-hexane at 1.7K. *Journal of Luminescence* **2000**, *86*, 261–263.

(26) Kozankiewicz, B.; Aloshyna, M.; Gudmundsdottir, A. D.; Platz, M. S.; Orrit, M.; Tamarat, P. Zero-Field Splitting of the Electronic Ground and Lowest Excited Triplet States of 2,2-Dinaphthylcarbene in n -Hexane at 1.7 K. *The Journal of Physical Chemistry A* **1999**, *103*, 3155–3162.

(27) Anderson, R. J. M.; Kohler, B. E. Electron nuclear double resonance of triplet diphenylmethylene in *P* 21 benzophenone: Conformation and spin distribution. *The Journal of Chemical Physics* **1976**, *65*, 2451–2459.

(28) Graham, D. J.; Wang, C.-L. A magnetic field study of excited triplet diphenylmethylene. *The Journal of Chemical Physics* **1986**, *85*, 4441–4445.

(29) Haider, K. W.; Platz, M. S.; Despres, A.; Lejeune, V.; Migirdicyan, E. Triplet-triplet fluorescence and spin polarization: diphenylcarbene and dibenzocycloheptadienylidene. *The Journal of Physical Chemistry* **1990**, *94*, 142–147.

(30) Wasserman, E.; Kuck, V. J.; Yager, W. A.; Hutton, R. S.; Greene, F. D.; Abegg, V. P.; Weinshenker, N. M. Electron paramagnetic resonance of 9,9'-dianthrylmethylene. Linear aromatic ground-state triplet methylene. *Journal of the American Chemical Society* **1971**, *93*, 6335–6337.

(31) Graham, D. J.; Lin, T.-S. High-Resolution Absorption Spectra of Diphenylmethylenes. *Chemical Physics* **1982**, 411–420.

(32) Brusar, V.; Forjan, M.; Ljubić, I.; Alešković, M.; Becker, K.; Vdović, S. Ultrafast Photoelimination of Nitrogen from Upper Excited States of Diazoalkanes and

the Fate of Carbenes Formed in the Reaction. *The Journal of Organic Chemistry* **2023**, *88*, 4286–4300.

(33) Piteša, T.; Alešković, M.; Becker, K.; Basarić, N.; Došlić, N. Photoelimination of Nitrogen from Diazoalkanes: Involvement of Higher Excited Singlet States in the Carbene Formation. *Journal of the American Chemical Society* **2020**, *142*, 9718–9724.

(34) Kawano, M.; Hirai, K.; Tomioka, H.; Ohashi, Y. Structure Determination of Triplet Diphenylcarbenes by in Situ X-ray Crystallographic Analysis. *Journal of the American Chemical Society* **2007**, *129*, 2383–2391.

(35) Chung, L. W.; Sameera, W. M. C.; Ramozzi, R.; Page, A. J.; Hatanaka, M.; Petrova, G. P.; Harris, T. V.; Li, X.; Ke, Z.; Liu, F.; Li, H.-B.; Ding, L.; Morokuma, K. The ONIOM Method and Its Applications. *Chemical Reviews* **2015**, *115*, 5678–5796.

(36) Frisch, M. J. et al. Gaussian 16 Rev. C.01. 2016.

(37) Shirazi, R. G.; Pantazis, D. A.; Neese, F. Performance of density functional theory and orbital-optimised second-order perturbation theory methods for geometries and singlet–triplet state splittings of arylcarbenes. *Molecular Physics* **2020**, *118*, e1764644.

(38) Neese, F.; Wennmohs, F.; Becker, U.; Riplinger, C. The ORCA quantum chemistry program package. *The Journal of Chemical Physics* **2020**, *152*, 224108.

(39) Neese, F. Software update: The ORCA program system—Version 5.0. *WIREs Computational Molecular Science* **2022**, *12*, e1606.

(40) Roos, B. O. In *Advances in Chemical Physics*, 1st ed.; Lawley, K. P., Ed.; Wiley, 1987; Vol. 69; pp 399–445.

(41) Angeli, C.; Cimiraglia, R.; Evangelisti, S.; Leininger, T.; Malrieu, J.-P. Introduction of n -electron valence states for multireference perturbation theory. *The Journal of Chemical Physics* **2001**, *114*, 10252–10264.

(42) Angeli, C.; Cimiraglia, R.; Malrieu, J.-P. n -electron valence state perturbation theory: A spinless formulation and an efficient implementation of the strongly contracted and of the partially contracted variants. *The Journal of Chemical Physics* **2002**, *117*, 9138–9153.

(43) Angeli, C.; Cimiraglia, R.; Malrieu, J.-P. N-electron valence state perturbation theory: a fast implementation of the strongly contracted variant. *Chemical Physics Letters* **2001**, *350*, 297–305.

(44) Roemelt, M.; Maganas, D.; DeBeer, S.; Neese, F. A combined DFT and restricted open-shell configuration interaction method including spin-orbit coupling: Application to transition metal L-edge X-ray absorption spectroscopy. *The Journal of Chemical Physics* **2013**, *138*, 204101.

(45) Poh, Y. R.; Chen, X.; Cheng, H.-P.; Yuen-Zhou, J. Electron Sextets as Optically Addressable Molecular Qubits: Triplet Carbenes. 2025; `https://chemrxiv.org/engage/chemrxiv/article-details/67ad478f6dde43c908a631aa`.

(46) Marian, C. M. Understanding and Controlling Intersystem Crossing in Molecules. *Annual Review of Physical Chemistry* **2021**, *72*, 617–640.

(47) Richert, S.; Tait, C. E.; Timmel, C. R. Delocalisation of photoexcited triplet states probed by transient EPR and hyperfine spectroscopy. *Journal of Magnetic Resonance* **2017**, *280*, 103–116.

(48) Miao, K. C.; Blanton, J. P.; Anderson, C. P.; Bourassa, A.; Crook, A. L.; Wolfowicz, G.; Abe, H.; Ohshima, T.; Awschalom, D. D. Universal coherence

protection in a solid-state spin qubit. *Science* **2020**, *369*, 1493–1497.

(49) Stoll, S.; Schweiger, A. EasySpin, a comprehensive software package for spectral simulation and analysis in EPR. *Journal of Magnetic Resonance* **2006**, *178*, 42–55.

(50) Ermolaev, V. L. The influence of deuteration of complex organic molecules on their fluorescence quantum yield (a review). *Optics and Spectroscopy* **2016**, *121*, 567–584.

(51) Fidy, J.; Laberge, M.; Kaposi, A. D.; Vanderkooi, J. M. Fluorescence line narrowing applied to the study of proteins. *Biochimica et Biophysica Acta (BBA) - Protein Structure and Molecular Enzymology* **1998**, *1386*, 331–351.

(52) Robledo, L.; Childress, L.; Bernien, H.; Hensen, B.; Alkemade, P. F. A.; Hanson, R. High-fidelity projective read-out of a solid-state spin quantum register. *Nature* **2011**, *477*, 574–578.

(53) Jelezko, F.; Gaebel, T.; Popa, I.; Gruber, A.; Wrachtrup, J. Observation of Coherent Oscillations in a Single Electron Spin. *Physical Review Letters* **2004**, *92*, 076401.

(54) Balasubramanian, G.; Neumann, P.; Twitchen, D.; Markham, M.; Kolesov, R.; Mizuochi, N.; Isoya, J.; Achard, J.; Beck, J.; Tissler, J.; Jacques, V.; Hemmer, P. R.; Jelezko, F.; Wrachtrup, J. Ultralong spin coherence time in isotopically engineered diamond. *Nature Materials* **2009**, *8*, 383–387.

(55) Yamamoto, T. et al. Extending spin coherence times of diamond qubits by high-temperature annealing. *Physical Review B* **2013**, *88*, 075206.

(56) Kanai, S.; Awschalom, D. D.; Ohno, H. Generalized scaling of spin qubit coherence in over 12,000 host materials. *PNAS* **2022**, *119*, e2121808119.

(57) Stepanov, V.; Takahashi, S. Determination of nitrogen spin concentration in diamond using double electron-electron resonance. *Physical Review B* **2016**, *94*.

(58) Thiele, S.; Balestro, F.; Ballou, R.; Klyatskaya, S.; Ruben, M.; Wernsdorfer, W. Electrically driven nuclear spin resonance in single-molecule magnets. *Science* **2014**, *344*, 1135–1138.

(59) Sipahigil, A. et al. An integrated diamond nanophotonics platform for quantum-optical networks. *Science* **2016**, *354*, 847–850.

(60) Kubo, Y.; Ong, F. R.; Bertet, P.; Vion, D.; Jacques, V.; Zheng, D.; Dréau, A.; Roch, J.-F.; Auffeves, A.; Jelezko, F.; Wrachtrup, J.; Barthe, M. F.; Bergonzo, P.; Esteve, D. Strong Coupling of a Spin Ensemble to a Superconducting Resonator. *Physical Review Letters* **2010**, *105*, 140502.

(61) Amsüss, R.; Koller, C.; Nöbauer, T.; Putz, S.; Rotter, S.; Sandner, K.; Schneider, S.; Schramböck, M.; Steinhauser, G.; Ritsch, H.; Schmiedmayer, J.; Majer, J. Cavity QED with magnetically coupled collective spin states. *Physical Review Letters* **2011**, *107*, 060502.

TOC Graphic

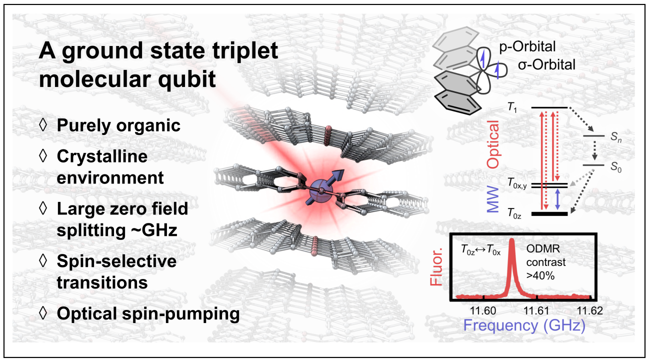
A ground state triplet molecular qubit
◊ Purely organic
◊ Crystalline environment
◊ Large zero field splitting ~GHz
◊ Spin-selective transitions
◊ Optical spin-pumping
p-Orbital
σ-Orbital
T_1
S_n
S_0
Optical
$T_{0x,y}$
MW
T_{0z}
Fluor.
T_{0z}↔T_{0x}
ODMR contrast >40%
11.60
11.61
11.62
Frequency (GHz)